EFFECT OF POROSITY PARAMETERS ON THE STATIC BUCKLING BEHAVIOR OF FGP PLATES USING THE RITZ METHOD AND FIRST-ORDER SHEAR DEFORMATION THEORY

Le Cao Tuan[1], Do Minh Duc[1]*, Tran Quang Hung[1], Tran Minh Tu[2]

[1]The University of Danang - University of Science and Technology, Vietnam
[2]Hanoi University of Civil Engineering, Vietnam

*Corresponding author: dmduc@dut.udn.vn

(Received: March 15, 2026; Revised: May 06, 2026; Accepted: June 05, 2026)

DOI: 10.31130/ud-jst.2026.24(7B).579E

Abstract - This study investigates the static buckling behavior of functionally graded porous (FGP) plates. A theoretical model is developed based on the first-order shear deformation theory (FSDT), while the Ritz method is utilized to solve the governing equations. In this model, the material properties are considered to vary continuously through according to three distinct porosity schemes, including uniform, symmetric, and asymmetric distributions. The validity and accuracy of the developed model are confirmed by benchmarking the results against available data reported in the literature. A comprehensive numerical study is carried out to explore the effects of key parameters, such as porosity characteristics (distribution patterns and coefficients) and geometric properties, on the critical buckling load. The outcomes of this investigation contribute to a better understanding and serve as a valuable resource for the design and optimization of engineering structures fabricated from advanced functional materials.

Key words - FGP plate; Ritz method; first-order shear deformation theory; static buckling behavior

1. Introduction

Functionally Graded Materials (FGMs) were introduced in the 1980s to overcome delamination and stress concentration phenomena commonly encountered in laminated composites, thereby enhancing the thermo-mechanical performance of structures subjected to complex loading conditions. Distinct from conventional multilayer composites, FGMs are defined by a smooth and continuous distribution of material characteristics across the thickness rather than discrete layer-wise variations. They are typically composed of two primary constituent phases, such as metal and ceramic, whose gradual transition effectively mitigates interfacial stress discontinuities and improves load-carrying capacity under severe service environments [1, 2]. Comprehensive review studies by Birman and Byrd [3] and Suresh and Mortensen [4] have further established the critical role of FGMs in advanced structural and multifunctional engineering applications.

In recent years, functionally graded porous (FGP) materials, considered a new class of FGMs, have been developed. These materials have attracted considerable research interest because their porosity can be controlled to achieve good strength-to-weight performance. In these materials, porosity is intentionally incorporated into the microstructure, introducing an additional design parameter that enables further tailoring of structural behavior. However, the presence of pores inevitably reduces the effective elastic modulus, thereby significantly influencing the stiffness characteristics and critical buckling loads of plate structures [5]. Consequently, the effect of porosity distribution and porosity coefficients has attracted significant attention in the optimal design of advanced graded structural materials.

Plate structures made of FGP materials have significant applications in aerospace, marine, and civil engineering fields. Static buckling under in-plane compressive loading constitutes a fundamental design requirement for such structural components, as buckling failure typically occurs prior to the material reaching its ultimate strength. Numerous studies have been conducted to investigate the mechanical response of FGP plates by means of various theoretical models and analytical approaches. For instance, Akbaş [6] investigated the static and dynamic analyses of FGP plates based on FSDT. Leclaire et al. [7] investigated the bending vibrations of thin FGP plates using the classical plate theory (CPT). Rezaei and Saidi [8] analyzed the free vibration of thick FGP plates based on the higher-order shear deformation theory (HSDT). Xiang et al. [9] employed Biot's poroelasticity theory to investigate the dynamic characteristics of rectangular FGP plates under various boundary conditions. Based on HSDT and Biot's poroelasticity theory, Arani et al. [10] calculated the natural frequencies of rectangular FGP plates resting on a Pasternak elastic foundation. Extending the application of advanced numerical techniques to porous sandwich structures, Hung and Tu [11] developed a mesh-free formulation for the geometrically nonlinear bending analysis of FGM porous sandwich beams.

Although numerous studies have been conducted on the analysis of FGP plates, there has been no study on the buckling analysis of FGP plates. Furthermore, no existing work has applied the Ritz method combined with FSDT to analyze of this type of structure. Therefore, the development of a buckling analysis model for FGP plates using the Ritz method in conjunction with FSDT is necessary and possesses significant scientific and practical importance.

This study aims to provide a comprehensive investigation into the static buckling characteristics of FGP plates through a computational framework using FSDT and the Ritz method. The proposed formulation employs trigonometric admissible functions to accurately satisfy different boundary conditions.

Moreover, detailed parametric analyses are performed to examine how porosity distributions, porosity coefficients, geometric ratios, and boundary conditions affect the critical buckling loads of FGP plates.

2. Basis formulations.

2.1. Geometry and mechanical properties of the FGP plate

2.1.1. Geometry of the FGP plate

Consider an FGP plate with in-plane dimensions $a \times b$ and thickness of h. The base material is characterized by the Young's modulus E_0 and Poisson's ratio υ. In this study, the FGP plate is analyzed considering three different porosity distribution patterns through the thickness, namely: uniform distribution (FGP-U), symmetric distribution (FGP-S), and asymmetric distribution (FGP-A), as depicted in Figure 1.

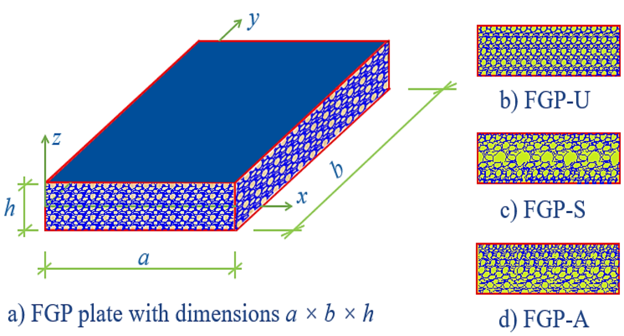

Figure 1. *FGP plate and its porosity distribution patterns*

2.1.2. Material properties of FGP plate

Effective Young's modulus for different porosity distributions [12, 13]

$$E(z)=\begin{cases} E_o\dfrac{4}{\pi^2}\left(\dfrac{\pi}{2}-1+\sqrt{1-e_o}\right)^2 & \text{(FGP-U)},\\ E_o\left(1-e_o\cos\left(\pi z/h\right)\right) & \text{(FGP-S)},\\ E_o\left(1-e_o\cos\left(0.5\pi z/h+\pi/4\right)\right) & \text{(FGP-A)}, \end{cases} \quad (1)$$

in which e_0 represents the porosity coefficient $\left(0\le e_0<1\right)$. The Poisson's ratio υ is assumed to be constant.

2.2. Formulation based on FSDT

2.2.1. Assumed displacement field

According to FSDT, the displacement components of the plate can be written as follows [14]:

$$\boldsymbol{d}=\begin{Bmatrix} u^*(x,y,z)\\ v^*(x,y,z)\\ w^*(x,y,z)\end{Bmatrix}=\begin{Bmatrix} u_0^*(x,y)+z\psi_x^*(x,y)\\ v_0^*(x,y)+z\psi_y^*(x,y)\\ w_0^*(x,y)\end{Bmatrix},$$

$$\boldsymbol{d}=\begin{bmatrix}1&0&0&z&0\\0&1&0&0&z\\0&0&1&0&0\end{bmatrix}\begin{Bmatrix}u_0^*\\v_0^*\\w_0^*\\\psi_x^*\\\psi_y^*\end{Bmatrix}=\mathbf{\Phi}_1\mathbf{A}_1, \quad (2)$$

where:

$$\mathbf{\Phi}_1=\begin{bmatrix}1&0&0&z&0\\0&1&0&0&z\\0&0&1&0&0\end{bmatrix},\ \mathbf{A}_1^{\mathrm{T}}=\left\{u_0^*\quad v_0^*\quad w_0^*\quad \psi_x^*\quad \psi_y^*\right\},$$

in Eq. (2) u_0^*, v_0^*, w_0^* denote the displacement components of a generic point on the mid-surface along the x, y, z directions, respectively; meanwhile, ψ_x^*, ψ_y^* describe the rotations of the normal to the mid-surface about the x and y axes, respectively. Quantities written in boldface are expressed in matrix form.

2.2.2. Relations between strain and displacement

The strain components are derived from the displacement–strain relations as follows:

$$\boldsymbol{\varepsilon}=\begin{Bmatrix}\varepsilon_{xx}^*\\\varepsilon_{yy}^*\\\gamma_{xy}^*\\\gamma_{xz}^*\\\gamma_{yz}^*\end{Bmatrix}=\begin{Bmatrix}u_{,x}^*\\v_{,y}^*\\u_{,y}^*+v_{,x}^*\\w_{,x}^*+u_{,z}^*\\w_{,y}^*+v_{,y}^*\end{Bmatrix}=\mathbf{\Phi}_2\mathbf{A}_2, \quad (3)$$

where:

$$\mathbf{\Phi}_2=\begin{bmatrix}1&0&0&0&0&0&0&0&z&0&0&0\\0&1&0&0&0&0&0&0&0&z&0&0\\0&0&0&0&1&1&0&0&0&0&z&z\\0&0&1&0&0&0&1&0&0&0&0&0\\0&0&0&1&0&0&0&1&0&0&0&0\end{bmatrix},$$

$$\mathbf{A}_2^T=\left\{u_{0,x}^*\ v_{0,y}^*\ w_{0,x}^*\ w_{0,y}^*\ u_{0,y}^*\ v_{0,x}^*\ \psi_x^*\ \psi_y^*\ \psi_{x,x}^*\ \psi_{y,y}^*\ \psi_{x,y}^*\ \psi_{y,x}^*\right\}.$$

The comma (,) used with displacement components refers to partial differentiation relative to the corresponding variable.

2.2.3. Stress–strain formulation based on Hooke's law

According to Hooke's law for linear elasticity, the stress components are determined from the strain field as follows:

$$\boldsymbol{\sigma}=\begin{Bmatrix}\sigma_{xx}^*\\\sigma_{yy}^*\\\tau_{xy}^*\\\tau_{xz}^*\\\tau_{yz}^*\end{Bmatrix}=\underbrace{\begin{bmatrix}Q_{11}^*&Q_{12}^*&0&0&0\\Q_{21}^*&Q_{22}^*&0&0&0\\0&0&Q_{33}^*&0&0\\0&0&0&Q_{44}^*&0\\0&0&0&0&Q_{55}^*\end{bmatrix}}_{\mathbf{E}_b}\underbrace{\begin{Bmatrix}\varepsilon_{xx}^*\\\varepsilon_{yy}^*\\\gamma_{xy}^*\\\gamma_{xz}^*\\\gamma_{yz}^*\end{Bmatrix}}_{\boldsymbol{\varepsilon}}=\mathbf{E}_b\boldsymbol{\varepsilon}, \quad (4)$$

where: $$\begin{cases} Q_{11}^*=Q_{22}^*=\dfrac{E(z)}{1-\upsilon^2};\ Q_{12}^*=Q_{21}^*=Q_{11}^*\upsilon=\dfrac{\upsilon E(z)}{1-\upsilon^2}\\ Q_{33}^*=G=\dfrac{E(z)}{2(1+\upsilon)};\ Q_{44}^*=Q_{55}^*=k_sQ_{33}^*. \end{cases}$$

k_s denotes the shear correction factor, which is assumed to be equal to 5/6; υ is the Poisson's ratio.

2.2.4. Governing equilibrium equations

a. The variation of the strain energy

$$\delta U_p = \int \delta\boldsymbol{\varepsilon}^{\mathrm{T}}\boldsymbol{\sigma} dV = \int \delta\boldsymbol{\varepsilon}^{\mathrm{T}}\mathbf{E}_{\mathrm{b}}\boldsymbol{\varepsilon} dV = \int \delta\mathbf{A}_2^{\mathrm{T}}\boldsymbol{\Phi}_2^{\mathrm{T}}\mathbf{E}_{\mathrm{b}}\boldsymbol{\Phi}_2\mathbf{A}_2 dV, \quad (5)$$

where: $\mathbf{N}_{\mathrm{E}} = \int_{-h/2}^{h/2} \boldsymbol{\Phi}_2^{\mathrm{T}}\mathbf{E}_{\mathrm{b}}\boldsymbol{\Phi}_2 dz.$

By substituting $\mathbf{N}_{\mathrm{E}}$ into Eq. (5), we obtain:

$$\delta U_p = \int_A \delta\mathbf{A}_2^{\mathrm{T}}\mathbf{N}_{\mathrm{E}}\mathbf{A}_2 dA. \quad (6)$$

b. The variation of virtual work done by in-plane loads

$$\delta V = \int_A \left(N_{xx}^0 \frac{\partial w_0^*}{\partial x}\frac{\partial \delta w_0^*}{\partial x} + 2N_{xy}^0 \frac{\partial w_0^*}{\partial x}\frac{\partial \delta w_0^*}{\partial y} + N_{yy}^0 \frac{\partial w_0^*}{\partial y}\frac{\partial \delta w_0^*}{\partial y} \right) dA. \quad (7)$$

The buckling response of FGP plates under uniformly distributed in-plane loads (as illustrated in Figure 2) on the plate edges in the x- and y- directions is analyzed:

- Along the edges $x = 0$, a: $N_{xx}^0 = \gamma_1 N_0$; $N_{xy}^0 = 0$;

- Along the edges $y = 0$, b: $N_{yy}^0 = \gamma_2 N_0$; $N_{xy}^0 = 0$;

where γ_1 and γ_2 are the in-plane load factors defining the biaxial loading ratios on the x- and y-directions, respectively.

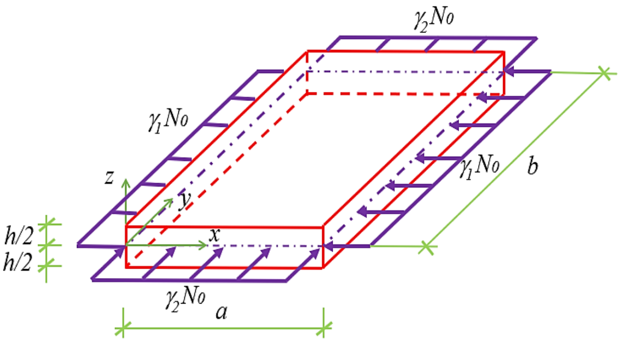

Figure 2. *FGP plate under in-plane loads applied on the mid-surface*

The equations of motion of the plate are established through Hamilton's principle, expressed mathematically as follows [15]:

$$\delta U_p + \delta V = 0. \quad (8)$$

2.2.5. Ritz formulation

In the Ritz method, the displacement expressions are generally represented as follows:

$$\begin{cases} u_0^*(x,y) = \sum_{k=1}^{K}\sum_{l=1}^{L} \varphi_{kl}^u a_{kl} = \boldsymbol{\varphi}_{kl}^u(x,y)\mathbf{a}^T, \\ v_0^*(x,y) = \sum_{k=1}^{K}\sum_{l=1}^{L} \varphi_{kl}^v b_{kl} = \boldsymbol{\varphi}_{kl}^v(x,y)\mathbf{b}^T, \\ w_0^*(x,y) = \sum_{k=1}^{K}\sum_{l=1}^{L} \varphi_{kl}^w c_{kl} = \boldsymbol{\varphi}_{kl}^w(x,y)\mathbf{c}^T, \\ \psi_x^*(x,y) = \sum_{k=1}^{K}\sum_{l=1}^{L} \varphi_{kl}^x d_{kl} = \boldsymbol{\varphi}_{kl}^x(x,y)\mathbf{d}^T, \\ \psi_y^*(x,y) = \sum_{k=1}^{K}\sum_{l=1}^{L} \varphi_{kl}^y e_{kl} = \boldsymbol{\varphi}_{kl}^y(x,y)\mathbf{e}^T. \end{cases} \quad (9)$$

$$\text{where: } \begin{cases} \mathbf{a} = \{a_{11} \quad a_{12} \quad a_{13} \quad \dots \quad a_{KL}\}, \\ \mathbf{b} = \{b_{11} \quad b_{12} \quad b_{13} \quad \dots \quad b_{KL}\}, \\ \mathbf{c} = \{c_{12} \quad c_{12} \quad c_{31} \quad \dots \quad c_{KL}\}, \\ \mathbf{d} = \{d_{11} \quad d_{12} \quad d_{13} \quad \dots \quad d_{KL}\}, \\ \mathbf{e} = \{e_{11} \quad e_{12} \quad e_{13} \quad \dots \quad e_{KL}\}; \end{cases}$$

$\mathbf{a}, \mathbf{b}, \mathbf{c}, \mathbf{d}, \mathbf{e}$ are the unknown variables to be determined; $\boldsymbol{\varphi}_{kl}^u, \boldsymbol{\varphi}_{kl}^v, \boldsymbol{\varphi}_{kl}^w, \boldsymbol{\varphi}_{kl}^x, \boldsymbol{\varphi}_{kl}^y$ are the functions satisfying the boundary conditions.

By inserting Eq. (9) into Eqs. (6), (7), and subsequently applying Eq. (8), the following expressions are obtained:

$$\left[\mathbf{K}_{\mathrm{e}} + N_0\mathbf{K}_g\right]\mathbf{q} = \mathbf{0}, \quad (10)$$

where $\mathbf{K}_{\mathrm{e}}$ represents the plate stiffness matrix, which is given by

$$\mathbf{K}_{\mathrm{e}} = \iint_A \mathbf{B}^{\mathrm{T}}\mathbf{N}_{\mathrm{E}}\mathbf{B} dA, \quad (11)$$

$$\mathbf{B} = \begin{bmatrix} \boldsymbol{\varphi}_{,x}^u & \mathbf{0} & \mathbf{0} & \mathbf{0} & \mathbf{0} \\ \mathbf{0} & \boldsymbol{\varphi}_{,y}^v & \mathbf{0} & \mathbf{0} & \mathbf{0} \\ \mathbf{0} & \mathbf{0} & \boldsymbol{\varphi}_{,x}^w & \mathbf{0} & \mathbf{0} \\ \mathbf{0} & \mathbf{0} & \boldsymbol{\varphi}_{,y}^w & \mathbf{0} & \mathbf{0} \\ \boldsymbol{\varphi}_{,y}^u & \mathbf{0} & \mathbf{0} & \mathbf{0} & \mathbf{0} \\ \mathbf{0} & \boldsymbol{\varphi}_{,x}^v & \mathbf{0} & \mathbf{0} & \mathbf{0} \\ \mathbf{0} & \mathbf{0} & \mathbf{0} & \boldsymbol{\varphi}^x & \mathbf{0} \\ \mathbf{0} & \mathbf{0} & \mathbf{0} & \mathbf{0} & \boldsymbol{\varphi}^y \\ \mathbf{0} & \mathbf{0} & \mathbf{0} & \boldsymbol{\varphi}_{,x}^x & \mathbf{0} \\ \mathbf{0} & \mathbf{0} & \mathbf{0} & \mathbf{0} & \boldsymbol{\varphi}_{,y}^y \\ \mathbf{0} & \mathbf{0} & \mathbf{0} & \boldsymbol{\varphi}_{,y}^x & \mathbf{0} \\ \mathbf{0} & \mathbf{0} & \mathbf{0} & \mathbf{0} & \boldsymbol{\varphi}_{,x}^y \end{bmatrix}; \quad (12)$$

and $\mathbf{K}_{\mathrm{g}}$ denotes the plate geometric stiffness matrix, which is given by

$$\mathbf{K}_g = \iint_A \begin{bmatrix} \mathbf{0} & \mathbf{0} & \mathbf{0} & \mathbf{0} & \mathbf{0} \\ \mathbf{0} & \mathbf{0} & \mathbf{0} & \mathbf{0} & \mathbf{0} \\ \mathbf{0} & \mathbf{0} & \gamma_1\left(\boldsymbol{\varphi}_{,x}^w\right)^2 + \gamma_2\left(\boldsymbol{\varphi}_{,x}^w\right)^2 & \mathbf{0} & \mathbf{0} \\ \mathbf{0} & \mathbf{0} & \mathbf{0} & \mathbf{0} & \mathbf{0} \\ \mathbf{0} & \mathbf{0} & \mathbf{0} & \mathbf{0} & \mathbf{0} \end{bmatrix} dA \quad (13)$$

$$\mathbf{q} = \{\mathbf{a} \quad \mathbf{b} \quad \mathbf{c} \quad \mathbf{d} \quad \mathbf{e}\}^{\mathrm{T}}.$$

2.2.6. Approximation functions for boundary conditions [16, 17]

According to the Ritz method, various admissible functions can be used. In this study, trigonometric functions are employed, which are selected to ensure satisfaction of the following boundary conditions.

***a.* Four edges are simply supported and free to move in the in-plane directions (SSSS)**

- At $x = 0$ and $x = a$: $v_0^* = 0$, $w_0^* = 0$, $\psi_y^* = 0$.

- At $y = 0$ and $y = b$: $u_0^* = 0$, $w_0^* = 0$, $\psi_x^* = 0$.

The approximation functions are chosen such that they satisfy the BCs of the SSSS plate [16, 17].

$$\begin{aligned}
u_0^*(x,y) &= \sum_{k=1}^{K}\sum_{l=1}^{L}\cos\left((2k-1)\pi x/a\right)\sin\left((2l-1)\pi y/b\right)a_{kl},\\
v_0^*(x,y) &= \sum_{k=1}^{K}\sum_{l=1}^{L}\sin\left((2k-1)\pi x/a\right)\cos\left((2l-1)\pi y/b\right)b_{kl},\\
w_0^*(x,y) &= \sum_{k=1}^{K}\sum_{l=1}^{L}\sin\left((2k-1)\pi x/a\right)\sin\left((2l-1)\pi y/b\right)c_{kl},\\
\psi_x^*(x,y) &= \sum_{k=1}^{K}\sum_{l=1}^{L}\cos\left((2k-1)\pi x/a\right)\sin\left((2l-1)\pi y/b\right)d_{kl},\\
\psi_y^*(x,y) &= \sum_{k=1}^{K}\sum_{l=1}^{L}\sin\left((2k-1)\pi x/a\right)\cos\left((2l-1)\pi y/b\right)e_{kl}.
\end{aligned} \tag{14}$$

b. Symmetric boundary condition with two simply supported edges and two clamped edges (SCSC)

- At $x = 0$ and $x = a$: $v_0^* = 0,\ w_0^* = 0,\ \psi_y^* = 0.$

- At $y = 0$ and $y = b$. $u_0^* = 0,\ w_0^* = 0,\ \psi_x^* = 0,\ w_{0,y}^* = 0.$

$$\begin{aligned}
u_0^*(x,y) &= \sum_{k=1}^{K}\sum_{l=1}^{L}\sin\left(2k\pi x/a\right)\sin\left((2l-1)\pi y/b\right)a_{kl},\\
v_0^*(x,y) &= \sum_{k=1}^{K}\sum_{l=1}^{L}\sin\left((2k-1)\pi x/a\right)\cos\left(2l\pi y/b\right)b_{kl},\\
w_0^*(x,y) &= \sum_{k=1}^{K}\sum_{l=1}^{L}\sin\left((2k-1)\pi x/a\right)\sin^2\left(l\pi y/b\right)c_{kl},\\
\psi_x^*(x,y) &= \sum_{k=1}^{K}\sum_{l=1}^{L}\cos\left((2k-1)\pi x/a\right)\sin^2\left(l\pi y/b\right)d_{kl},\\
\psi_y^*(x,y) &= \sum_{k=1}^{K}\sum_{l=1}^{L}\sin\left((2k-1)\pi x/a\right)\sin\left(2l\pi y/b\right)e_{kl}.
\end{aligned} \tag{15}$$

c. Four edges of the plate are fully clamped (CCCC)

- At $x = 0$ and $x = a$: $v_0^* = 0,\ w_0^* = 0,\ \psi_y^* = 0,\ w_{0,x}^* = 0.$

- At $y = 0$ and $y = b$: $u_0^* = 0,\ w_0^* = 0,\ \psi_x^* = 0,\ w_{0,y}^* = 0.$

$$\begin{aligned}
u_0^*(x,y) &= \sum_{k=1}^{K}\sum_{l=1}^{L}\sin\left(2k\pi x/a\right)\sin\left((2l-1)\pi y/b\right)a_{kl},\\
v_0^*(x,y) &= \sum_{k=1}^{K}\sum_{l=1}^{L}\sin\left((2k-1)\pi x/a\right)\cos\left(2l\pi y/b\right)b_{kl},\\
w_0^*(x,y) &= \sum_{k=1}^{K}\sum_{l=1}^{L}\sin^2\left(k\pi x/a\right)\sin^2\left(l\pi y/b\right)c_{kl},\\
\psi_x^*(x,y) &= \sum_{k=1}^{K}\sum_{l=1}^{L}\sin\left(2k\pi x/a\right)\sin^2\left(l\pi y/b\right)d_{kl},\\
\psi_0^*(x,y) &= \sum_{k=1}^{K}\sum_{l=1}^{L}\sin^2\left(k\pi x/a\right)\sin\left(2l\pi y/b\right)e_{kl}.
\end{aligned} \tag{16}$$

In Eqs. (14)-(16), K and L indicate the numbers of trigonometric basis functions, while k, l = 1, 2, 3… Each pair of integers (k, l) corresponds to a specific buckling mode. The critical buckling load follows from the condition that Eq. (10) admits a non-trivial solution $\mathbf{q} \neq \mathbf{0}$, given by:

$$\det\left(\mathbf{K}_e + N_0\mathbf{K}_g\right) = 0. \tag{17}$$

The solution of this equation gives $N_0 = N_{kl}$, which defines the buckling load related to the mode (k, l). The critical buckling load is then determined as the minimum value among all buckling loads. Hence, $N_{cr} = \min\{N_{kl}\}$.

3. Numerical results and discussion

3.1. Model validation

For the numerical investigation, a computational code was developed in Matlab to implement the formulation based on the FSDT. To validate the correctness of the theoretical derivation and numerical implementation, an isotropic plate is considered, corresponding to an FGP plate with a porosity coefficient e_0 = 0. In this case, material properties are chosen as $E_0 = 70\times10^3$ MPa, $\upsilon = 0.3$.

For convenience and to facilitate comparison with previously published results, the following non-dimensional quantities are employed [18]:

$$\overline{N} = N_{cr}\frac{a^2}{\pi^2 D},\quad D = \frac{E_0 h^3}{12\left(1-\upsilon^2\right)}. \tag{18}$$

The validation example is conducted by evaluating the critical buckling load of a SSSS square isotropic plate with side-to-thickness ratio a/h = 5 and 10, as reported in Table 1. The present results, obtained via the Ritz method within the framework of FSDT, are benchmarked against those reported by Shufrin and Eisenberger [18]. The study in Ref. [18] also adopted the FSDT approach in conjunction with the extended Kantorovich method. The present Ritz solutions show excellent agreement with the reference results, which can be attributed to the fact that both methods are based on FDST, thereby confirming the reliability and effectiveness of the proposed model.

Table 1. *Non-dimensional critical buckling load $\overline{N}$ of a square isotropic plate (FGP with e_0 =0)*

γ_1, γ_2	a/h	Shufrin, Eisenberger [18]	**Present**	Deviation
(−1,0)	10	3.7865	**3.7865**	0.00
	5	3.2637	**3.2637**	0.00
(0,−1)	10	3.7865	**3.7865**	0.00
	5	3.2637	**3.2637**	0.00
(−1,−1)	10	1.8932	**1.8932**	0.00
	5	1.6319	**1.6319**	0.00

3.2. Parametric study

This subsection examines FGP plates with different BCs, such as SSSS, SCSC, and CCCC. The base material is assumed to be aluminum (Al), with $E_0 = 70\times10^3$ MPa and $\upsilon = 0.3$.

3.2.1. Effect of the porosity coefficient e_0 on the critical buckling load

The results presented in Table 2 and Figures 3 to 6 demonstrate that $\overline{N}$ decreases with increasing e_0 for all BCs and all porosity distribution patterns, when e_0 = 0.5 the non-dimensional critical buckling load of the FGP-U plate decreases to 66.18% of that corresponding to e_0 = 0 for SSSS; this tendency originates from the degradation of the effective Young's modulus along the thickness as the porosity coefficient increases, which causes a decrease in the equivalent bending stiffness and consequently diminishes the buckling resistance of the plate. For a given plate type and a fixed value of e_0, the critical buckling load increases in the order SSSS < SCSC < CCCC; for instance, the FGP-U plate with $e_0 = 0.5$ the non-dimensional critical buckling load for SSSS is only 40.83% of that corresponding to the same plate with CCCC; where stiffer boundary constraints enhance the overall structural rigidity and thus elevate the critical load. Moreover, under identical boundary conditions and the same porosity coefficient e_0, the FGP-S configuration consistently yields higher critical buckling loads than the FGP-U and FGP-A configurations. This confirms that the through-thickness material distribution directly influences the effective bending stiffness. Locating higher-modulus material farther from the neutral axis increases the bending stiffness contribution, thereby significantly improving the stability performance of the plate.

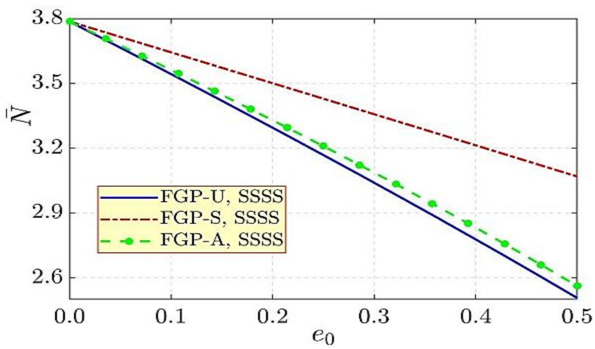

Figure 3. *Non-dimensional critical buckling load $\overline{N}$ of different FGP plate types versus the porosity coefficient e_0 for SSSS*

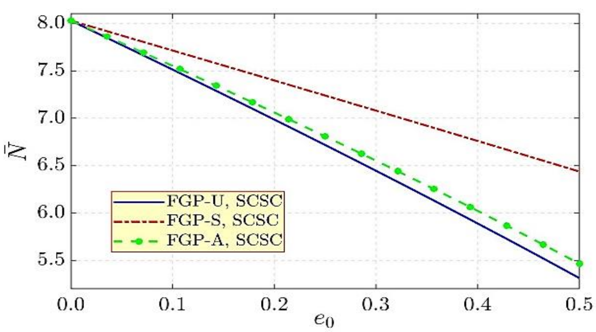

Figure 4. *Non-dimensional critical buckling load $\overline{N}$ of different FGP plate types versus the porosity coefficient e_0 for SCSC*

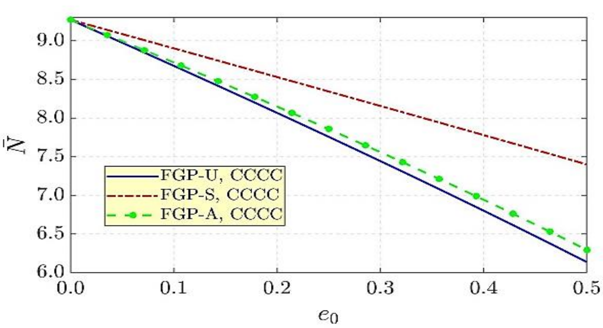

Figure 5. *Non-dimensional critical buckling load $\overline{N}$ loads of different FGP plate types versus the porosity coefficient e_0 for CCCC*

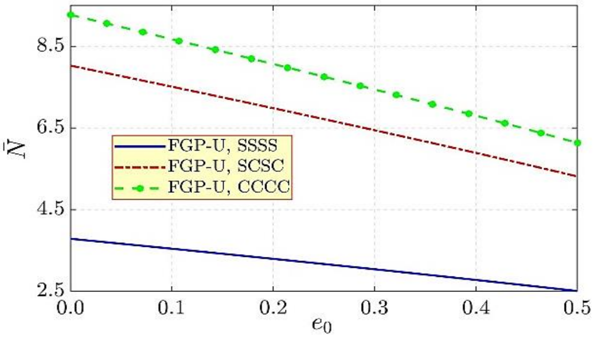

Figure 6. *Non-dimensional critical buckling load $\overline{N}$ of different FGP plate types versus the porosity coefficient e_0 for different BCs*

Table 2. *Non-dimensional critical buckling load $\overline{N}$ of a square FGP plate ($a/h = 10$, $\gamma_1 = -1$, $\gamma_2 = 0$) different the porosity coefficient e_0 for various BCs*

BCs	Porosity distribution patterns	e_0			
		0	0.1	0.3	0.5
SSSS	FGP-U	3.7865	3.5431	3.0399	2.506
	FGP-S	3.7865	3.6438	3.3572	3.0685
	FGP-A	3.7865	3.5619	3.0869	2.5616
SCSC	FGP-U	8.0287	7.5127	6.4458	5.3137
	FGP-S	8.0287	7.7139	7.0798	6.437
	FGP-A	8.0287	7.5514	6.5522	5.4657
CCCC	FGP-U	9.2722	8.6763	7.4441	6.1367
	FGP-S	9.2722	8.9026	8.1571	7.3999
	FGP-A	9.2722	8.7194	7.5597	6.2942

3.2.2. Effect of the side-to-thickness ratio a/h

The results presented in Table 3 and Figures 7 to 9 indicate that the non-dimensional critical buckling load increases as a/h increases from 10 to 100 for all BCs and all types of FGP plates (FGP-U, FGP-S, and FGP-A). When $a/h \geq 50$, the variation of this critical load with respect to a/h becomes negligible. This trend can be attributed to the reduced effect of transverse shear deformation as the plate becomes increasingly thin.

Table 3. *Non-dimensional critical buckling load $\overline{N}$ of square FGP plates ($e_0 = 0.3$, $\gamma_1 = -1$, $\gamma_2 = 0$) versus the a/h ratio for different BCs*

BCs	Porosity distribution patterns	a/h			
		10	30	50	100
SSSS	FGP-U	3.0399	3.1914	3.2041	3.2096
	FGP-S	3.3572	3.5414	3.557	3.5636
	FGP-A	3.0869	3.2419	3.255	3.2606
SCSC	FGP-U	6.4458	7.1294	7.1906	7.2168
	FGP-S	7.0798	7.9056	7.9804	8.0125
	FGP-A	6.5522	7.2527	7.3156	7.3424
CCCC	FGP-U	7.4441	8.4229	8.5124	8.5508
	FGP-S	8.1571	9.337	9.4463	9.4932
	FGP-A	7.5597	8.5625	8.6543	8.6937

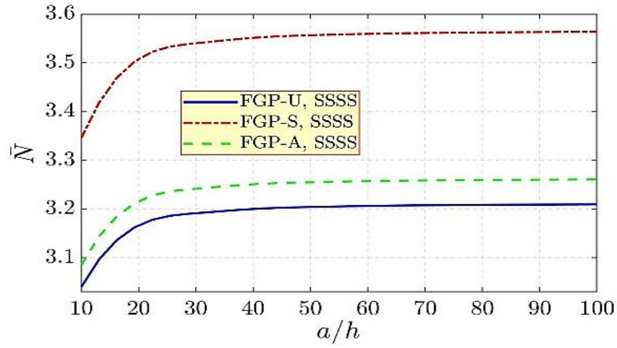

Figure 7. *Non-dimensional critical buckling load* $\overline{N}$ *of FGP plate versus the a/h ratio for SSSS plates*

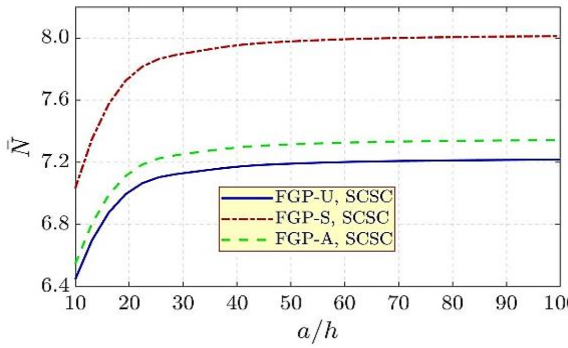

Figure 8. *Non-dimensional critical buckling load* $\overline{N}$ *of FGP plate versus the a/h ratio for SCSC*

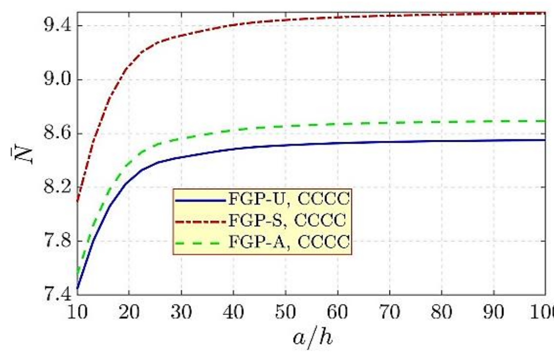

Figure 9. *Non-dimensional critical buckling load* $\overline{N}$ *of FGP plate versus the a/h ratio for CCCC*

3.2.3. Effect of the aspect ratio b/a

Table 4. *Non-dimensional critical buckling load* $\overline{N}$ *of square FGP plates (*$e_0 = 0.3$*, a/h =10,* $\gamma_1 = -1$*,* $\gamma_2 = 0$*) versus the aspect ratio b/a for different BCs*

BCs	Porosity distribution patterns	*b/a* 1	2	3	5
SSSS	FGP-U	3.0399	1.2117	0.9611	0.8436
	FGP-S	3.3572	1.3408	1.0638	0.9340
	FGP-A	3.0869	1.2307	0.9761	0.8568
SCSC	FGP-U	6.4458	1.5383	1.0579	0.8694
	FGP-S	7.0798	1.7008	1.1708	0.9625
	FGP-A	6.5522	1.57	1.0821	0.8907
CCCC	FGP-U	7.4441	3.5392	3.1323	2.9663
	FGP-S	8.1571	3.8889	3.4422	3.2600
	FGP-A	7.5597	3.5946	3.1811	3.0124

The results presented in Table 4 and Figures 10 to 12 demonstrate that $\overline{N}$ decreases markedly as the geometric ratio *b/a* increases for all BCs and all porosity distribution patterns. This decline is mainly due to the increase in the effective plate length in the buckling direction, which reduces the overall structural stiffness and, consequently, the buckling resistance.

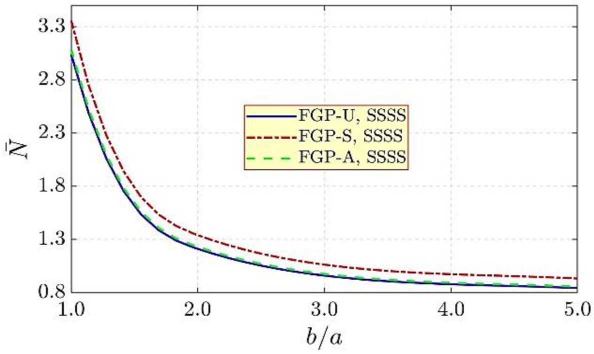

Figure 10. *Non-dimensional critical buckling load* $\overline{N}$ *of FGP plates versus the aspect ratio b/a for SSSS*

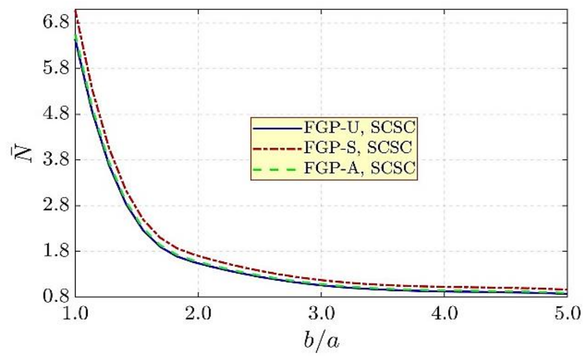

Figure 11. *Non-dimensional critical buckling load* $\overline{N}$ *of FGP plates versus the aspect ratio b/a for SCSC*

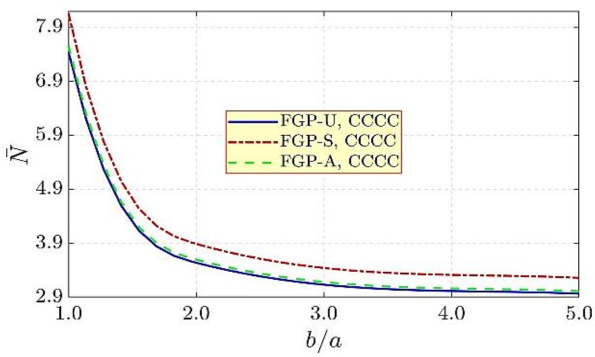

Figure 12. *Non-dimensional critical buckling load* $\overline{N}$ *of FGP plates versus the aspect ratio b/a for CCCC*

4. Conclusions

This paper investigates the influence of porosity distribution patterns, porosity coefficients and geometrical parameters on critical buckling load of FGP plates under various BCs. Some main conclusions derived from the numerical results are as follows:

The critical buckling load decreases with increasing porosity coefficient e_0 for all BCs and all porosity distribution patterns.

For a given plate type and identical geometric parameters, the critical buckling load increases in the order SSSS < SCSC < CCCC confirming that stiffer edge constraints enhance the overall structural rigidity and thus improve buckling resistance.

Among the porosity distribution patterns considered, the FGP-S configuration consistently yields the highest critical buckling load in all investigated cases. This finding confirms that the through-thickness porosity distribution plays a decisive role in determining the effective bending stiffness.

The non-dimensional critical buckling load increases with an increase in the side-to-thickness ratio a/h. For thin plates (a/h >50), the variation this critical buckling load becomes negligible.

An increase in the aspect ratio b/a leads to a marked reduction in the critical buckling load. The results highlight the significant impact of in-plane geometric proportions on the buckling characteristics of FGP plates.

REFERENCES

[1] J. Reddy, "Analysis of functionally graded plates," *International Journal for numerical methods in engineering*, vol. 47, no. 1-3, pp. 663-684, 2000.

[2] H.-S. Shen, *Functionally graded materials: nonlinear analysis of plates and shells.* CRC press, 2016.

[3] V. Birman and L. W. Byrd, "Modeling and analysis of functionally graded materials and structures," *Applied Mechanics Reviews*, vol. 60, no. 5, pp. 195–216, 2007.

[4] S. Suresh and A. Mortensen, "*Fundamentals of Functionally Graded Materials, IOM Commun*," Ltd, Cambridge, 1998.

[5] D. Chen, "Static and dynamic analysis of functionally graded porous structures," Ph.D. dissertation, School of Civil Engineering, The University of Queensland, Brisbane, QLD, Australia, 2018.

[6] Ş. D. Akbaş, "Vibration and static analysis of functionally graded porous plates," *Journal of Applied and Computational Mechanics,* vol. 3, no. 3, pp. 199-207, 2017.

[7] P. Leclaire, K. Horoshenkov, and A. Cummings, "Transverse vibrations of a thin rectangular porous plate saturated by a fluid," *Journal of Sound and Vibration*, vol. 247, no. 1, pp. 1-18, 2001.

[8] A. Rezaei and A. Saidi, "Exact solution for free vibration of thick rectangular plates made of porous materials," *Composite Structures,* vol. 134, pp. 1051-1060, 2015.

[9] Y. Xiang, H. Jiang, and J. Lu, "Analyses of dynamic characteristics of a fluid-filled thin rectangular porous plate with various boundary conditions," *Acta Mechanica Solida Sinica*, vol. 30, no. 1, pp. 87-97, 2017.

[10] A. G. Arani, Z. Khoddami Maraghi, M. Khani, and I. Alinaghian, "Free Vibration of Embedded Porous Plate Using Third-Order Shear Deformation and Poroelasticity Theories," *Journal of Engineering,* vol. 2017, no. 1, p. 1474916, 2017.

[11] T. Q. Hung and T. M. Tu, "Geometrically nonlinear bending mesh-free analysis of functionally graded porous sandwich beam," *The University of Danang - Journal of Science and Technology*, vol. 21, no. 6.1, pp. 16-21, 2023. doi:10.31130/ud-jst.2023.091E.

[12] D. Chen, J. Yang, and S. Kitipornchai, "Free and forced vibrations of shear deformable functionally graded porous beams," *International journal of mechanical sciences,* vol. 108, pp. 14-22, 2016.

[13] M. R. Barati and A. M. Zenkour, "Investigating post-buckling of geometrically imperfect metal foam nanobeams with symmetric and asymmetric porosity distributions," *Composite Structures,* vol. 182, pp. 91-98, 2017.

[14] J. N. Reddy, *Theory and analysis of elastic plates and shells*. CRC press, 2006.

[15] J. N. Reddy, *Energy principles and variational methods in applied mechanics.* John Wiley & Sons, 2017.

[16] M. Sobhy, "Buckling and free vibration of exponentially graded sandwich plates resting on elastic foundations under various boundary conditions," *Composite Structures,* vol. 99, pp. 76-87, 2013.

[17] M. A. A. Meziane, H. H. Abdelaziz, and A. Tounsi, "An efficient and simple refined theory for buckling and free vibration of exponentially graded sandwich plates under various boundary conditions," *Journal of Sandwich Structures & Materials,* vol. 16, no. 3, pp. 293-318, 2014.

[18] I. Shufrin and M. Eisenberger, "Stability and vibration of shear deformable plates–first order and higher order analyses," *International journal of solids and structures,* vol. 42, no. 3-4, pp. 1225-1251, 2005